Photothermal bleaching in time-lapse photoacoustic microscopy

Liang Gao, Lidai Wang, Chiye Li, Alejandro Garcia-Uribe, and Lihong V. Wang †
Optical Imaging Laboratory, Department of Biomedical Engineering, Washington University in St. Louis., St. Louis, MO 63130, USA
†LHWANG@WUSTL.EDU

ABSTRACT

We studied the phenomenon of photothermal bleaching — a gradual reduction of contrast agent particles during repeated scans in photoacoustic microscopy. The dependence of the photothermal bleaching rate on the excitation pulse energy was determined while the laser focal diameter was held constant. Our results showed that, the dependence of the photothermal bleaching rate on the excitation pulse energy differed before and after the absorbers were raised to their melting point by the deposited laser energy. Based on this finding, we suggested an optimal excitation pulse energy, which balances the photothermal bleaching rate and signal amplitude, for time-lapse imaging applications.
Keywords: photoacoustic microscopy, photothermal bleaching

1. INTRODUCTION

Photobleaching, a common phenomenon in fluorescence microscopy, occurs when a fluorophore permanently loses its ability to fluoresce due to long exposure to intense excitation light [1, 2]. On the one hand, photobleaching undesirably limits the observation time for monitoring a dynamic process; on the other hand, photobleaching can be beneficially employed in molecular diffusion or motion studies via techniques such as fluorescence-recovery after photobleaching (FRAP) [3, 4] or fluorescence loss in photobleaching (FLIP) [5]. Properly exploiting photobleaching requires a thorough understanding of its dependence on the excitation light power. Such a dependence in fluorescence microscopy has been carefully characterized [1, 2, 6].

However, photobleaching is not exclusively a feature of fluorescence microscopy: It also exists in other imaging modalities. One example is photoacoustic microscopy (PAM) [7-9], in which the sample is irradiated by a short laser pulse (~ns duration). The absorbed light energy is converted into heat and produces an ultrasonic wave via thermoelastic expansion. The ultrasonic wave is detected by an ultrasound transducer. Contrasts in PAM stem from light absorption by endogenous or exogenous absorbers, such as hemoglobin [10] or nanoparticles [11, 12], respectively. These absorbers can be intentionally photo-destructed using strong excitation light, resulting in a gradual reduction of photoacoustic signals during repeated scans.

The photobleaching mechanism in PAM differs from that in fluorescence microscopy. Upon absorbing a photon, an electron transits from the ground state to an excited state. The electron's energy can be released via primarily two paths: radiative decay, *i.e.*, fluorescence, or non-radiative decay, *i.e.*, thermal dissipation. In fluorescence microscopy, photobleaching is the photochemical destruction of a fluorophore – during radiative decay the excited electrons are trapped in a relatively long-lived triplet state (lifetime ~ 1 μs), thus allowing the fluorophore a much longer time to undergo irreversible chemical reactions with the environment than would be allowed by the singlet-singlet transition [13]. In PAM, photobleaching is the photothermal destruction of an absorber – the heat generated during non-radiative decay alters the structure of the absorber, thus reducing sample's absorption coefficient at the original excitation wavelength. To distinguish the photobleaching in PAM from its fluorescent counterpart, we term this photothermally induced absorption change as "photothermal bleaching".

To begin to exploit the photothermal bleaching in PAM, here we studied its dependence on the laser pulse energy while the laser focal diameter was held constant. GNPs were chosen as the targets because they were widely used as contrast agents in photoacoustic imaging applications [11, 12, 14]. Our results revealed that, within the linear excitation range, photothermal bleaching behaved differently before and after the GNPs were raised to their melting point. Below this critical point, the photothermal bleaching rate had weak dependence on the laser pulse energy; while above the melting point, the photothermal bleaching rate increased rapidly. Based on this finding, we suggest a method to determine the optimal excitation laser pulse energy for time-lapse photoacoustic imaging.

Photons Plus Ultrasound: Imaging and Sensing 2014, edited by Alexander A. Oraevsky, Lihong V. Wang,
Proc. of SPIE Vol. 8943, 89433G · © 2014 SPIE · CCC code: 1605-7422/14/$18 · doi: 10.1117/12.2038564

2. MATERIALS AND METHODS

2.1 Sample preparation

To eliminate the effect of diffusion during the photothermal bleaching rate measurement, the target GNPs were fixed on top of cover glasses by the following operations [15-17]. The cover glasses were first cleaned in warm detergent (RBS 35, Sigma-Aldrich, USA), flushed with DI water, and dried with nitrogen. Then the cover glasses were put in a plasma oxidizer (Diener Electronics, Germany) for 20 min, followed by another 20 min in a 10% solution of (3-Aminopropyl)-triethoxysilane (Sigma-Aldrich, USA) in anhydrous ethanol. After silanization, the cover glasses were rinsed in anhydrous ethanol and kept at 120 ^{o}C for 3 hours. Gold particles with mean diameters of 50 nm, 70 nm, 100 nm (TedPella, USA) and 400 nm (Cytodiagnostics, Canada) were pipetted onto the silanized cover glasses and baked in a 45 ^{o}C oven overnight. Before imaging, the samples were washed with DI water on a shaker for 3 hours to remove the unfixed residual gold particles.

2.2 Time-resolved measurement of photothermal bleaching dynamics

Time-resolved photothermal bleaching experiments were performed using a previously described voice-coil scanning PAM [18] with 0.1 NA optical objective. The PAM uses a raster-scanned focused ultrasonic transducer coupled with confocal optical illumination to detect light-absorption-induced ultrasound signals. Two 532-nm-wavelength pulsed lasers (Elforlight, Ltd., UK), with 1 ns and 10 ns pulse durations, respectively, were employed in the photothermal bleaching experiments. The excitation laser pulse energy was adjusted by rotating a variable ND filter (Thorlabs Inc., USA) in front of the laser output, and monitored by a custom-made photodiode. Before the experiment, the correspondence between the laser pulse energy at the sample and the photodiode's measured value was calibrated.

During the photothermal bleaching experiments, the sample was continuously scanned by the PAM at 0.5 Hz C-scan rate until the signals vanished from the image. The image was acquired with 1000 voice coil scanning steps and 20 mechanical stage scanning steps, and rendered as a maximum amplitude projection image. The photoacoustic amplitude of an image was calculated by summing all the signals within the field-of-view (400 × 100 μm^2) after removing the background. The photothermal bleaching rate k was calculated by fitting a double exponential curve $A\exp(-k_1 t) + B\exp(-k_2 t)$ to the acquired data and averaging over the exponential indices $k = Ak_1 + Bk_2$ [6, 19].

3. RESULTS AND DISCUSSION

To confine our studies within the linear photoacoustic imaging range, where the photoacoustic signal amplitude is proportional to the laser pulse energy, we first identified the pulse energy range for linear excitation. GNPs of 400 nm in diameter were suspended in water solution and imaged by a PAM system [18] using different pulse energies. Since GNPs diffuse freely in the water solution, the photothermally bleached particles were rapidly replaced, and thus negligible. The measured photoacoustic amplitude versus laser pulse energy is shown in Fig. 1. Below ~120 nJ (fluence: 0.33 J/cm^2), photoacoustic amplitude is linearly related to the pulse energy, so laser pulse energies within this linear range were used in the following experiments. The focal diameter of the laser beam was set to 6.8 μm for all experiments, and the laser wavelength was 532 nm.

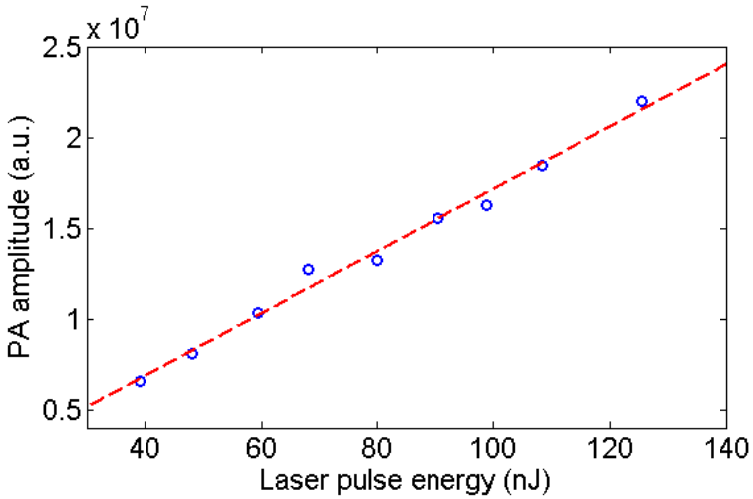

Fig. 1. Photoacoustic amplitude vs. delivered excitation laser pulse energy. The 400-nm-diameter GNPs were suspended in water solution and imaged by PAM. The coefficient of determination, R^2, was 0.990.

Next, the 400-nm-diameter GNPs were fixed on a cover glass to eliminate the effect of diffusion on the measurement of photothermal bleaching rate. The photoacoustic images acquired at time 0 second, 25 seconds, and 200 seconds are shown in Fig. 2. The GNPs were fragmented by the deposited laser energy during photoacoustic imaging and thus vanished. The photothermal bleaching dynamics were measured under different laser pulse energies, and the results are shown in Fig. 3. The photothermal bleaching rate k was calculated by fitting a double exponential curve to the acquired data.

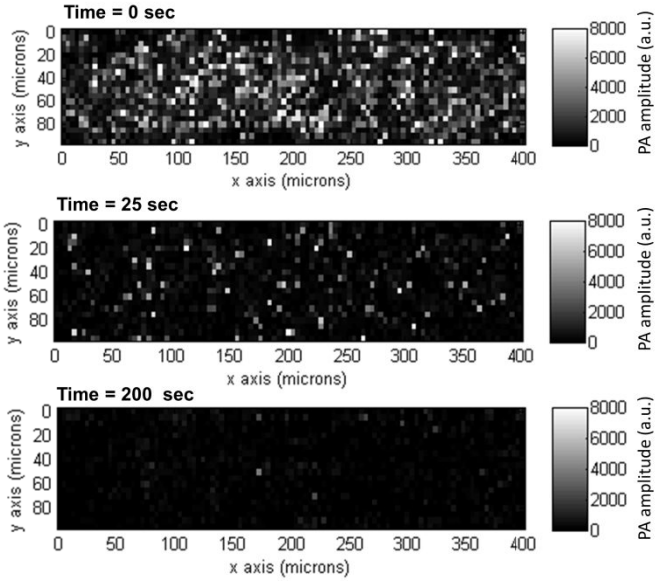

Fig. 2. Photothermal bleaching of gold nanoparticles (GNP) in time-lapse photoacoustic imaging. The GNPs were fragmented by the deposited laser energy during photoacoustic imaging and thus vanished.

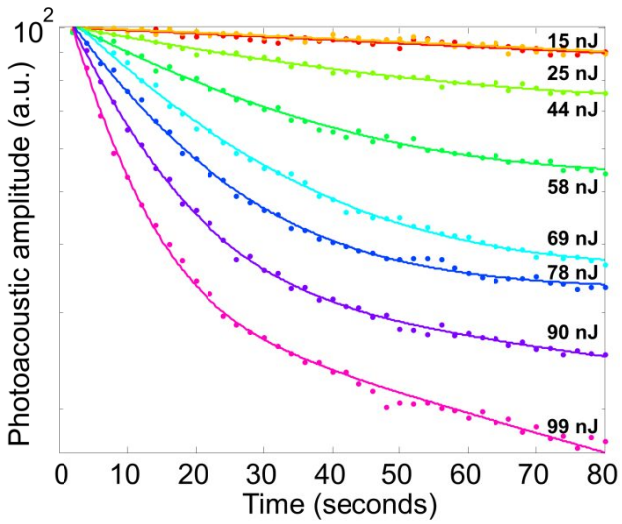

Fig. 3. Photothermal bleaching of 400-nm-diameter GNPs under different delivered laser pulse energies. The samples were continuously imaged by PAM at 0.5 Hz C-scan rate.

Fig. 4 is a log-log plot of photothermal bleaching rate versus laser pulse energy. Since the photothermal bleaching in PAM originates from instantaneous optical heating, we estimated the temperature rise of a GNP upon a pulse laser excitation and correlated it to the measured photothermal bleaching rate. The light absorption of a spherical GNP obeys Beer's law, which gives

$$\Delta E = \int F(1-e^{-\mu_a l})d\sigma = \int_0^{\pi/2} \frac{I}{A}(1-e^{-\mu_a D\cos\theta})\pi\frac{D^2}{4}\sin 2\theta d\theta\,, \tag{1}$$

where F is the optical fluence (J/cm^2), σ is the projected cross-section perpendicular to the incident light direction, l is the optical path length, μ_a is the absorption coefficient ($\mu_a^{Au} = 5.6867\times10^5$ cm^{-1}), D is the absorber's diameter, I is the laser pulse energy, A is the focal spot area, and θ is the polar angle in the spherical coordinates. Since the thermal confinement time for a 400 nm GNP in water solution is

$$\tau_{th} = \frac{d_c^2}{\alpha_{th}} = \frac{(0.4\times10^{-4}\,\text{cm})^2}{1.3\ \text{cm}^2/\text{s}} = 1.2\ \text{ns}\,, \tag{2}$$

(d_c is the characteristic dimension of the heated region, and α_{th} is the thermal diffusivity of gold), which is longer than the laser pulse duration (1 ns), the optical heating process was regarded as thermally confined, *i.e.*, thermal conduction was negligible during the pulse laser excitation. Consequently, the temperature rise of a GNP approximates

$$\Delta T = \frac{\Delta E}{C_V \rho V}\,, \tag{3}$$

where C_V is the specific heat ($C_V^{Au} = 0.13$ J/g.k), ρ is the mass density ($\rho^{Au} = 19.3$ g.cm^{-3}), and V is the volume. By substituting ΔE in Eq. 1 into Eq. 3, the temperature rise ΔT under the excitation of different pulse energies was calculated (Table 1).

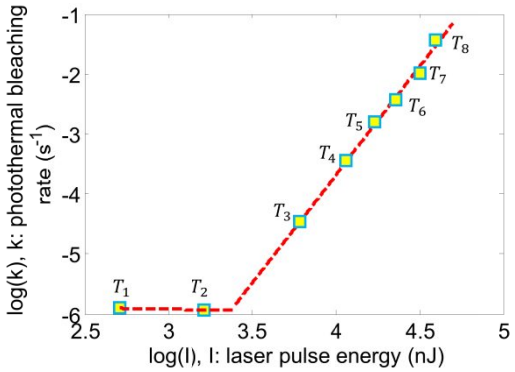

Fig. 4. Dependence of photothermal bleaching rate ***k*** on the delivered laser pulse energy and temperature rise. ***I*** is the laser pulse energy (nJ), and ***k*** is the photothermal bleaching rate (s^{-1}). The slope for the data points with pulse energies > 30 nJ is 3.6 ± 0.3 (95% confidence bounds). The coefficient of determination, R^2, is 0.996. The corresponding temperature rises T_i $(i = 1, 2, ..8)$ are calculated and shown in Table. 1.

Measurement index	Laser pulse energy (nJ)	Temperature rise (K)
1	15	483
2	25	806
3	44	1418
4	58	1869
5	69	2223
6	78	2513
7	90	2900
8	99	3190

Table 1. Calculated temperature rise of a 400 nm diameter GNP upon excitation by different laser pulse energies.

The data in Fig. 4 gives two slopes : below $I_c = 30$ nJ, the photothermal bleaching rate k has a weak dependence on the laser pulse energy; while above it, the slope equals 3.6 ± 0.3, indicating a nonlinear relation between photothermal bleaching rate and laser pulse energy – $k \propto I^{3.6}$. The corresponding temperature rise for the critical point $I_c = 30$ nJ was calculated by Eq. 1 and Eq. 3, yielding

$$\Delta T_c = 967K . \tag{4}$$

Assuming the room temperature was $23\ ^\circ C$, the temperature of the GNP after a pulse laser excitation approximated

$$T = T_{room} + \Delta T_c = 990\ ^\circ C , \tag{5}$$

close to the melting point of gold ($T^{Au}_{melting} = 1,064\ ^\circ C$). This implies that the phase change of the absorber (from solid to liquid state) may contribute to the two different photothermal bleaching behaviors observed within the linear PA excitation range.

Since photothermal bleaching behaves differently around an absorber's melting point under linear excitation, this dependence suggests an optimal excitation pulse energy for the time-lapse photoacoustic imaging: I_c, the critical value that raises the GNPs to their melting point. Below I_c, raising the excitation pulse energy increases the photoacoustic signal linearly but does not noticeably speed up the photothermal bleaching rate. While above I_c, although increasing the

excitation pulse energy can linearly improve the signal, the photothermal bleaching accelerates nonlinearly, significantly shortening the time window for imaging a dynamic event.

4. CONCLUSION

In summary, we studied the phenomenon of photothermal bleaching in PAM. The dependence of the photothermal bleaching rate on the excitation laser pulse energy was carefully measured and analyzed. Our results showed that, under linear photoacoustic excitation, two different photothermal bleaching behaviors exist around the absorber's melting point. Based on this finding, an optimal excitation laser pulse energy, which balances the strength of the photoacoustic signal and the bleaching rate, was suggested for time-lapse imaging applications.

To the best of our knowledge, this is the first time that the phenomenon of photothermal bleaching was characterized in PAM. This knowledge will be valuable not only for the GNP-based PA imaging, but also for establishing new photothermal-bleaching-assisted techniques such as photoacoustic-recovery after photothermal bleaching [20] or photoacoustic-loss in photothermal bleaching.

REFERENCES

1. R. I. Ghauharali, J. W. Hofstraat and G. J. Brakenhoff, "Fluorescence photobleaching-based shading correction for fluorescence microscopy," *J Microsc-Oxford* 192, 99-113 (1998)
2. R. I. Ghauharali and G. J. Brakenhoff, "Fluorescence photobleaching-based image standardization for fluorescence microscopy," *J Microsc-Oxford* 198, 88-100 (2000)
3. E. A. J. Reits and J. J. Neefjes, "From fixed to FRAP: measuring protein mobility and activity in living cells," *Nat Cell Biol* 3(6), E145-E147 (2001)
4. Y. H. Sniekers and C. C. van Donkelaar, "Determining diffusion coefficients in inhomogeneous tissues using fluorescence recovery after photobleaching," *Biophys J* 89(2), 1302-1307 (2005)
5. J. Lippincott-Schwartz, E. Snapp and A. Kenworthy, "Studying protein dynamics in living cells," *Nat Rev Mol Cell Bio* 2(6), 444-456 (2001)
6. G. H. Patterson and D. W. Piston, "Photobleaching in two-photon excitation microscopy," *Biophys J* 78(4), 2159-2162 (2000)
7. L. V. Wang, "Multiscale photoacoustic microscopy and computed tomography," *Nat Photonics* 3(9), 503-509 (2009)
8. L. H. V. Wang and S. Hu, "Photoacoustic Tomography: In Vivo Imaging from Organelles to Organs," *Science* 335(6075), 1458-1462 (2012)
9. V. L. Wang and L. Gao, "Photoacoustic microscopy and computed tomography: from bench to bedside " *Annu Rev Biomed Eng* (2014)
10. S. Hu and L. V. Wang, "Photoacoustic imaging and characterization of the microvasculature," *J Biomed Opt* 15(1), 011101 (2010)
11. Q. Zhang, N. Iwakuma, P. Sharma, B. M. Moudgil, C. Wu, J. McNeill, H. Jiang and S. R. Grobmyer, "Gold nanoparticles as a contrast agent for in vivo tumor imaging with photoacoustic tomography," *Nanotechnology* 20(39), 395102 (2009)
12. X. M. Yang, E. W. Stein, S. Ashkenazi and L. H. V. Wang, "Nanoparticles for photoacoustic imaging," *Wires Nanomed Nanobi* 1(4), 360-368 (2009)
13. R. Y. Tsien, L. Ernst and A. Waggoner, "Fluorophores for Confocal Microscopy: Photophysics and Photochemistry," in *Handbook Of Biological Confocal Microscopy* J. B. Pawley, Ed., Springer (2006).
14. S. Mallidi, T. Larson, J. Tam, P. P. Joshi, A. Karpiouk, K. Sokolov and S. Emelianov, "Multiwavelength Photoacoustic Imaging and Plasmon Resonance Coupling of Gold Nanoparticles for Selective Detection of Cancer," *Nano Lett* 9(8), 2825-2831 (2009)
15. C. George, D. Ricci and E. Di Zitti, "Gold nanoparticles self-assembled onto passivated glass substrates: Tuning the transition from 2D to 1D structures," *Superlattice Microst* 44(4-5), 608-616 (2008)
16. N. Nath and A. Chilkoti, "A colorimetric gold nanoparticle sensor to interrogate biomolecular interactions in real time on a surface," *Anal Chem* 74(3), 504-509 (2002)
17. G. Arslan, M. Özmen, B. Gündüz, X. Zhang and M. Ersöz, "Surface modification of glass beads with an aminosilane monolayer," *Turkish Journal of Chemistry* 30(2), 203-210 (2006)

18. L. D. Wang, K. Maslov, J. J. Yao, B. Rao and L. H. V. Wang, "Fast voice-coil scanning optical-resolution photoacoustic microscopy," *Optics Letters* 36(2), 139-141 (2011)
19. S. Gavrilyuk, S. Polyutov, P. C. Jha, Z. Rinkevicius, H. Agren and F. Gei'mukhanov, "Many-photon dynamics of photobleaching," *J Phys Chem A* 111(47), 11961-11975 (2007)
20. C. Y. Li, C. Zhang, L. Gao, A. Garcia-Uribe and L. H. V. Wang, "Photoacoustic recovery after photothermal bleaching in living cells," *J Biomed Opt* 18(10), 106004 (2013)